5 Measurements of radiation damage on silicon sensors

Editors: A. De Cosa[a], B. Nachman[b], P. Collins[c].
Contributing authors: J. L. Agram[d], W. Barter[e], M. Baselga[f], M. Battaglia[g], J. Beyer[h], H. M. Borecka-Bielska[i], D. Brzhechko[j], A. De Cosa[a], I. Dawson[k], F. Djama[l], F. Feindt[m], A. Grummer[n], M. Hoeferkamp[n], J. Hunt[f], T. Kondo[p], V. Lima[q], A. Macchiolo[j], J. Llorente Merino[s], K. Mochizuki[t], B. Nachman[b], G. Sarpis[u], S. Seidel[n], J. Sonneveld[v], S. Tsuno[p], M. Vignali[m], R. Wang[w].
[a]ETH Zurich, Switzerland
[b]Lawrence Berkeley National Laboratory, USA
[c]CERN, Geneva, Switzerland
[d]Hubert Curien Pluridisciplinary Institute (IPHC) Strasbourg - Univ. de Haute-Alsace, France
[e]Imperial College London, United Kingdom
[f]Karlsruhe Institute of Technology, Germany
[g]University of California, Santa Cruz, USA
[h]Ludwig Maximilian University of Munich, Germany
[i]University of Liverpool, United Kingdom
[j]University of Zurich, Switzerland
[k]Queen Mary University of London, United Kingdom
[l]CPPM, Marseille, France
[m]Hamburg University, Germany
[n]University of New Mexico, USA
[p]KEK, Tsukuba, Japan
[s]Institute of High Energy Physics, Beijing, China
[t]University of Montreal, Canada
[u]University of Manchester, United Kingdom
[v]Nikhef, Amsterdam, Netherlands
[w]Argonne National Laboratory, USA

Non-ionizing energy loss introduces defects in the silicon lattice that modify the electronic properties of the bulk material. See Section 2.1 for a detailed discussion. As a result, the sensor leakage current increases and the electric field from an applied bias voltage is distorted. Electron–hole pairs from a minimum ionizing particle traverse the modified electric field and can be trapped in the silicon lattice defects. Measuring and modelling these effects is essential for informing detector operations, monitoring the radiation environment near the detector, tuning offline simulation algorithms, and making performance predictions for the future.

Sensor damage is characterized by the particle fluence Φ and the goal of this section is to present measurements of a number of observables X and their response to Φ, $\mathrm{d}X/\mathrm{d}\Phi$. Comparing the responses of X across time is complicated by annealing effects and thermal histories across the detector systems can vary significantly. An additional complication is that the particle composition and energy spectra of the radiation backgrounds, discussed in Section 4, can vary substantially across different detector layers. Radiation damage in silicon is typically scaled to the 1 MeV neutron equivalent fluence ($\Phi_{\mathrm{eq}}^{\mathrm{Si}}$), but this assumes the NIEL hypothesis, see Section 2.1.1, which is not always respected. Additional challenges with sensor measurements and their interpretation are discussed in Section 5.4. Below are the observables that have been studied by one or more of the LHC experiments.

This chapter should be cited as: Measurements of radiation damage on sensors, Eds. A. De Cosa, B. Nachman, P. Collins, DOI: 10.23731/CYRM-2021-001.59, in: Radiation effects in the LHC experiments: Impact on detector performance and operation, Ed. Ian Dawson,
CERN Yellow Reports: Monographs, CERN-2021-001, DOI: 10.23731/CYRM-2021-001, p. 59.

1. *Leakage current*: the current measured across the sensor when applying a bias voltage independent of ionization from charged particles. The leakage current contributes to the noise and is relevant for module power consumption. This power will heat the module, which further increases the leakage current. In extreme cases, this can lead to *thermal runaway*, whereby the sensors quickly reach electrical breakdown.
2. *Depletion voltage*: the bias voltage such that nearly the entire sensor is depleted. After irradiation, the electric field can have regions of low field, so this concept is less well defined. It is usually measured by performing a high voltage scan and finding the point at which the collected charge, cluster size, or hit efficiency saturate. Unlike the leakage current, measuring the depletion voltage therefore usually requires active collisions in order to measure the collected charge. This is true for all subsequent measurements as well.
3. *Hit/Cluster efficiency*: the probability of minimum ionizing particle producing a signal in the sensor that is registered above threshold. Charge trapping shifts the deposited charge distribution to lower values and thus reduces the efficiency. The hit efficiency is the probability in a single sensor and the cluster efficiency is the probability for a particle going through a detector layer. Clusters are composed of multiple hits. It is more likely that hits on the periphery of a cluster goes below threshold than that the whole cluster is lost.
4. *Collected charge*: a direct measurement of the induced charge. Track reconstruction efficiency is most affected by the cluster efficiency, but the track parameters can also be impacted by the amount of collected charge. Furthermore, the charge itself is often used for particle identification, making use of the fact that heavier/slower particles ionize more than lighter/faster particles.
5. *Position resolution*: one of the direct consequences of losing hits on the periphery of a cluster is the degradation in the position resolution.
6. *Lorentz angle*: ionized electrons and holes drift in both the sensor electric field and the detector magnetic field. The track incidence angle that corresponds to the minimum transverse cluster size that results from the balance between these fields is called the Lorentz angle. The angle is largely insensitive to charge trapping, but can be used to study deformations in the sensor electric field.

This chapter is organized as follows. Section 5.1 introduces, for each experiment, aspects of the detector set-up and measurement methods particularly relevant for the measurements. Next, the models used to interpret the data are summarized in Section 5.2. Then, in Section 5.3, we present the measurements for the above observables. The chapter ends with discussion and outlook in Section 5.4.

5.1 Measurement considerations

5.1.1 ATLAS

Particle fluence cannot be measured directly. Instead, the luminosity is measured as explained in Section 3.2 and Monte Carlo simulations are used to convert this to a 1 MeV neutron equivalent fluence ($\Phi_{\mathrm{eq}}^{\mathrm{Si}}$). Another important input to many of the measurements and their interpretation is the sensor temperature. Temperatures are measured per module and stored in a conditions database. While these temperatures are measured as close as possible to the sensors, there is a potential offset. A summary of the operating conditions for the ATLAS pixel detector during Run 2 can be found in Fig. 36. The high voltage was slowly increased throughout the run in order to compensate for the raising depletion voltage (see Section 5.3).

5.1.2 CMS

Similarly to ATLAS, the fluence is inferred from the measured luminosity using FLUKA simulations, (CMS FLUKA study v3.23.1.0). Luminosity values are translated into charged and neutral particle

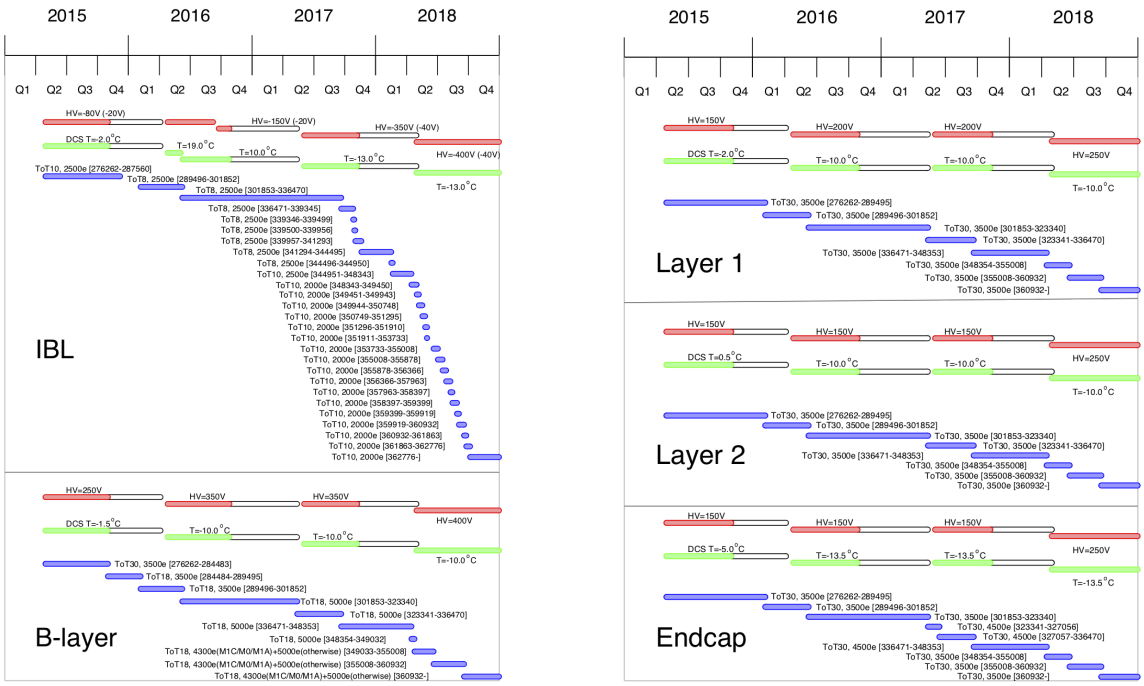

Fig. 36: The operating conditions of the ATLAS pixel detector during the LHC Run 2. The red bars indicate the high voltage setting, the green lines are the temperatures, and the blue bars represent the charge thresholds and periods where these were recalibrated. ToT stands for time over threshold, which is a digitized version of the deposited charge using either 4 (innermost layer) or 5 (outer layers) bits.

fluences at a given position in the CMS detector taking into account the proton–proton cross-section at the respective beam energy.

The other main source of uncertainty for the radiation damage tracker modelling is the measurement of the silicon sensor temperatures. In the pixel barrel, temperature measurements are taken along the cooling pipes, with temperature sensors mounted on the carbon fibre support structure at the edges of the barrel. The on-sensor temperature is estimated to be about 2–5 K higher than the temperatures measured on the support structures from studies on a thermal mockup. More details on the mock-up system and on the studies performed are discussed in Ref. [2]. The temperature in the CMS pixel detector is controlled by an evaporative CO_2 cooling system. During 2017 and 2018, the operation point of the cooling plant was set to $-22\,^{\circ}\mathrm{C}$. The coolant temperature decreases along the cooling lines due to a drop in the CO_2 pressure. This feature of the cooling system results in a temperature gradient inside the detector of up to $6\,^{\circ}\mathrm{C}$. This spread in temperature translates in a spread in leakage current values for modules placed at the same distance from the beam line: measurements for modules placed on a same layer differ up to a factor of 2. This effect was verified on the thermal mock-up as well, where a similar spread in temperature and leakage current measurements was observed. The forward pixel detector has on-module temperature sensors that provide measurements for each readout group (ROG).

Sensor temperature and leakage current measurements for the CMS strip detector are provided with high granularity: one measurement per module. Measurements can be retrieved from the detector control unit (DCU), an ASIC mounted on the front-end hybrid PCB. Figure 37 shows a map of the sensor temperatures within the CMS strip detector as measured during 2017 data taking from the DCUs.

The detector was operated at $-15\,^{\circ}\mathrm{C}$ during 2015–2017, and the temperature was lowered to $-20\,^{\circ}\mathrm{C}$ at the beginning of 2018 in order not to reach the power supply current limits in detector regions with degraded cooling contacts or passive cooling. During Run 3 several modules are expected to experience thermal runaway. Reducing further the coolant temperature to $-25\,^{\circ}\mathrm{C}$ will allow us to decrease this number by almost a factor of 2. Preliminary studies indicate that the detector will be able to provide good performance throughout Run 3.

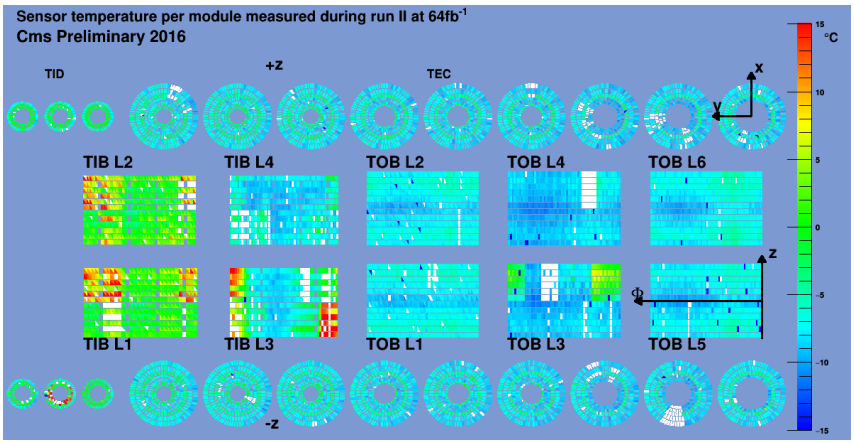

Fig. 37: Map of silicon temperature per module for the CMS strip detector, measured in 2017 at 68.4 fb^{-1} with coolant temperature at $-15\,^{\circ}\mathrm{C}$. White spots arise from modules which are not read out, or for which DCU readings are missing. Detector regions with missing direct cooling, or degraded cooling contacts show visibly higher temperatures with respect to the average.

5.1.3 LHCb

The LHCb VELO operated throughout Run 1 and Run 2 of the LHC (2011–2018) without changes to the sensor hardware. Due to its proximity to the proton beam, the sensors were exposed to a fluence of up to approximately 6.5×10^{14} 1MeV $\mathrm{n_{eq}}$ cm^2. As expected, this extreme radiation environment caused changes to the sensor material and performance via radiation damage effects.

To quantify the radiation damage effects, the estimated fluence accumulated by each sensor is calculated. This can be done by measuring the leakage currents in the silicon sensors, as they are expected to vary linearly with fluence [4]. The fluence is estimated from the simulation, known radiation damage factors and luminosity. A single current is measured for each VELO sensor, corresponding to the current drawn by the entire sensor. The difference of the measured currents amongst sensors is dominated by the variation in sensor temperatures, and to a lesser degree, by their distance to the interaction region.

5.2 Radiation damage modelling

There are two types of microscopically motivated effective radiation damage models used to interpret the measurements presented in subsequent sections. One set of models include annealing effects (Hamburg and Sheffield models) and the other set of models make predictions for deformations in the electric field inside the sensor. This second set of models are developed in the framework of technology computer aided design (TCAD) simulations. At the moment, there is no one framework for modelling both annealing and a non-trivial electric field inside the sensor bulk. Traditionally, annealing models are used to interpret the leakage current and depletion voltage data while TCAD simulations are used for observables that are related to track reconstruction. Integrating TCAD models into full detector systems is further discussed in Chapter 7.

5.2.1 *Leakage current modelling*

For a given instantaneous irradiation with fluence Φ, the leakage current changes as $\Delta I_{\text{leak}} = \alpha V \Phi$, where V is the depleted volume of the sensor and α is approximately independent of the damaging particle energies and flavours. After some time t at a temperature T, the leakage current changes from defect annealing, so $\alpha = \alpha(t, T)$. Different models vary in their treatment of α, including n_{states} effective defect states whose contribution to the leakage current evolves with time. In all models, the leakage current starting from zero current is given by

$$I_{\text{leak}} = (\Phi / L_{\text{int}}) \cdot \sum_{i=1}^{n} V_i \cdot L_{\text{int},i} \left[\sum_{j=1}^{n_{\text{states}}} \alpha_j \big((T_i, t_i), (T_{i+1}, t_{i+1}), ..., (T_n, t_n) \big) \right] , \tag{21}$$

where $L_{\text{int},i}$ is the integrated luminosity, V_i is the depleted volume, t_i is the duration, and T_i is the temperature in time interval i. The three most common forms for the α_j are as follows:

$$\begin{aligned} \alpha_1^A &= \alpha_I \exp\left(- \sum_{j=i}^{n} \frac{t_j}{\tau(T_j)} \right) \\ \alpha_2^A &= \alpha_0^* - \beta \log \left(\sum_{j=i}^{n} \frac{\Theta(T_j) \cdot t_j}{t_0} \right) , \end{aligned} \tag{22}$$

$$\begin{aligned} \alpha_1^B &= \alpha_1^A \\ \alpha_2^B &= \alpha_0 + \frac{1}{\sum_{j=1}^{n} t_j} \sum_{j=1}^{n} \frac{t_j}{T_j} - \beta \log \left(\sum_{j=i}^{n} \frac{t_j}{t_0} \right) , \end{aligned} \tag{23}$$

$$\alpha_k^C = \alpha(T_{\text{ref}}) \frac{A_k \tau_k}{\Theta(T_i) t_i} \left[1 - \exp\left(- \frac{\Theta(T_i) t_i}{\tau_k} \right) \right] \exp\left(- \frac{1}{\tau_k} \sum_{j=1}^{n} \Theta(T_j) t_j \right) , \tag{24}$$

where Eqs. 22 and 23 are called the Hamburg model [4] and Eq. 24 is called the Sheffield model [5]. Both Eqs. 22 and 23 assume that the annealing over time t with fixed temperature T is given by $\alpha \exp(-t/\tau) + \alpha_0 - \beta \log(t/t_0)$; they differ in how to treat periods with varying temperature. The unspecified functions in the above equations are $1/\tau(T) = k_{I,0} \exp(-E_i / k_B T)$ and $\Theta(T) = \exp(-E_i / k_B (1/T - 1/T_{\text{ref}}))$. Typical parameters are given in Tables 9 and 10. These are the values used by both the ATLAS and CMS pixel and strip detector groups [4, 6, 16]. Other values used in some measurements from LHCb can be found in Ref. [7]. An example implementation of the code can be found at this link: http://cern.ch/go/mDb9.

The resulting prediction is then valid for leakage currents measured at a value T_{ref}. In order to compare the data directly with this prediction, the data are corrected to correspond to the same constant reference temperature. This is done by using the following scaling factor:

$$\left(\frac{T_{\text{ref}}}{T} \right)^2 \exp\left(- \frac{E_{\text{eff}}}{2 k_B} \left(\frac{1}{T_{\text{ref}}} - \frac{1}{T} \right) \right) , \tag{25}$$

where E_{eff} is the effective band-gap energy in silicon. The most commonly used value of E_{eff} is 1.21 eV [8], but some studies have suggested that a lower value (e.g., 1.12 eV [6]) may lead to a better fit with collider data.

Table 9: Leakage current model parameters from Eq. 22 using Ref. [4].

Parameter	Value	Units
α_I	$(1.23 \pm 0.06) \times 10^{-17}$	A/cm
$k_{I,0}$	$1.2^{+5.3}_{-1.0} \times 10^{13}$	Hz
E_I	1.11 ± 0.05	eV
α_0^*	7.07×10^{-17}	A/cm
β	3.29×10^{-18}	A/cm
E_I^*	1.30 ± 0.14	eV
t_0	1	min.
T_{ref}	21	°C

Table 10: Leakage current model parameters from Eq. 24 using Ref. [5] using $T_{\text{ref}} = 20\,°\text{C}$. The value for $\alpha(T_{\text{ref}})$ is $(4.81 \pm 0.13) \times 10^{-17}$ A/cm.

k	τ_k (min)	A_k
1	$(1.2 \pm 0.2) \times 10^6$	0.42 ± 0.11
2	$(4.1 \pm 0.6) \times 10^4$	0.10 ± 0.01
3	$(3.7 \pm 0.3) \times 10^3$	0.23 ± 0.02
4	124 ± 2.5	0.21 ± 0.02
5	8 ± 5	0.04 ± 0.03

5.2.2 Full depletion voltage modelling

Aside from the V_i term in Eq. 21, modelling the leakage current is largely insensitive to the doping concentration spatial distribution inside the sensor. In contrast, the full depletion voltage becomes poorly defined when the electric field profile inside the sensor has a non-linear shape. For unirradiated sensors, one can relate the full depletion voltage and the effective doping concentration:

$$V_{\text{depl}} = |N_{\text{eff}}| \cdot \frac{ed^2}{2\epsilon\epsilon_0}\,, \tag{26}$$

where d is the sensor thickness, e is the unit charge, ϵ is the dielectric constant, and ϵ_0 is the vacuum permittivity. There currently does not exist a model that can account for both the spatial inhomogeneity of N_{eff} and its annealing. For predicting the operational full depletion voltage, experiments typically focus on the thermal effects. The most widely used model for this goal is the Hamburg model[3]:

$$N_{\text{eff}}(t,T) = N_{\text{D}}^{\text{non-removable}}(0) + N_{\text{D}}^{\text{removable}}(t) - N_{\text{A}}^{\text{stable}}(t) - N_{A}^{\text{beneficial}}(t,T) - N_{A}^{\text{reverse}}(t,T)\,, \tag{27}$$

where $N_{\text{D}}^{\text{(non)-removable}}(0)$ is the initial concentration of (non)-removable donors and the other terms are defined below. The fraction of removable donors for the typical concentrations used for LHC silicon sensors is predicted to be all of the initial doping concentration for charged-particle irradiation. Irradiation by charged particles dominates the damage on the innermost layers of the LHC experiments. The components of Eq. 27 are governed by coupled system of differential equations:

$$\begin{aligned}
\frac{\text{d}}{\text{d}t}N_{\text{D}}^{\text{removable}}(t) &= -c\phi(t)N_{\text{D}}^{\text{removable}}(t) && \text{removal of donors for } n\text{-type during irradiation,}\\
\frac{\text{d}}{\text{d}t}N_{\text{A}}^{\text{stable}}(t) &= g_{\text{C}}\phi(t) && \text{addition of stable acceptors during irradiation,}\\
\frac{\text{d}}{\text{d}t}N_{\text{A}}^{\text{beneficial}}(t,T) &= g_{\text{A}}\phi(t) - k_{\text{A}}(T)N_{\text{A}}^{\text{beneficial}}(t,T) && \text{beneficial annealing,}\\
\frac{\text{d}}{\text{d}t}N_{\text{N}}^{\text{reverse}}(t,T) &= g_{\text{Y}}\phi(t) - k_{\text{Y}}(T)N_{\text{N}}^{\text{reverse}}(t,T) && \text{reverse annealing – neutrals,}\\
\frac{\text{d}}{\text{d}t}N_{\text{A}}^{\text{reverse}}(t,T) &= k_{\text{Y}}(T)N_{\text{N}}^{\text{reverse}}(t,T) && \text{reverse annealing – acceptors,}
\end{aligned} \tag{28}$$

[3]Both the leakage current and full depletion voltage models are typically referred to as 'the' Hamburg model [4], but the physical parameters of the two models are not related.

where $\phi(t)$ is the irradiation rate in $n_{eq}/cm^2/s$ ($\Phi = \int dt\phi(t)$). The introduction rates have been measured by the ROSE collaboration [9] and typical values for the other parameters can be found in Ref. [4]. One challenge is that the ROSE collaboration measurements do not report uncertainties and also do not include charged hadron damage for g_A. Even though the damage is different for charged and neutral hadrons, typically experiments pick one value when simulating Eq. 27. An example implementation of the code can be found at this link: http://cern.ch/go/mDb9.

5.3 Results

5.3.1 Leakage current

5.3.1.1 ATLAS pixels

The ATLAS pixel system consists of four parts: the insertable B-layer (IBL), the outer barrel layers, and the endcaps. The IBL was added to the ATLAS detector at the start of Run 2, but has already accumulated more fluence than any other layer due to its close proximity to the interaction point (3.3 cm). Figure 38 presents the measured and simulated leakage current on the IBL as a function of the integrated luminosity during Run 2. The simulations have been fit with an overall scale factor (Φ/L_{int} in Eq. 21). The IBL is composed of four equally spaced module groups along the beam direction, z. The current is highest for the innermost module group and decreases monotonically to the fourth group. The outermost module group is composed of 3D sensors [10] which require a much lower bias voltage to be fully depleted. The right plot of Fig. 38 is the ratio of the innermost module groups to the 3D module group. The ratio is expected to be constant and proportional to the ratio of fluences. During 2016 (around 20 fb^{-1}), the innermost module groups were under-depleted, which is observed as a dip in the leakage current ratio.

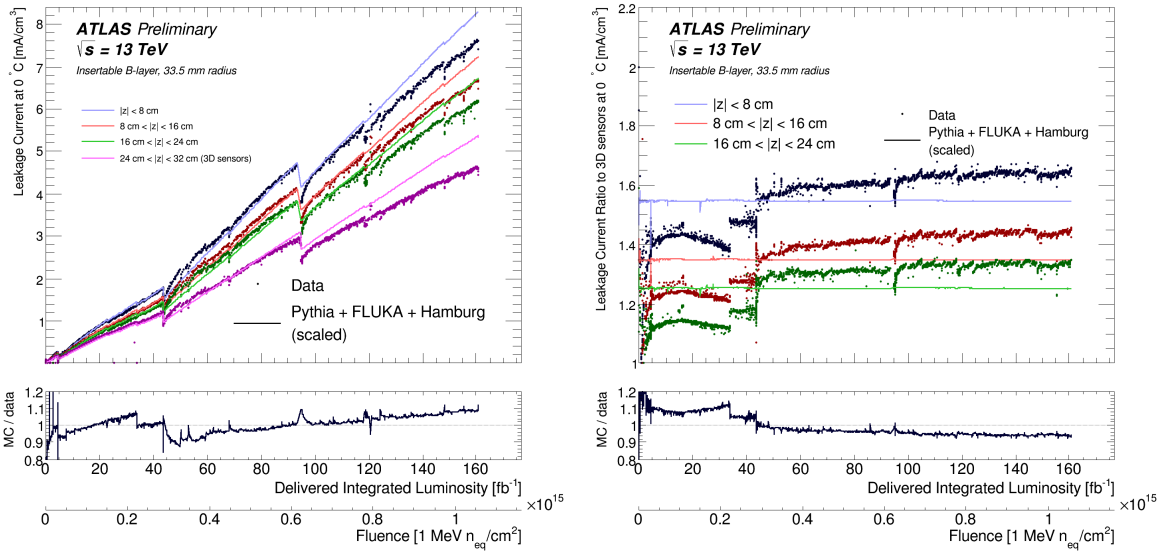

Fig. 38: The leakage current as a function of the integrated luminosity in Run 2 for the ATLAS IBL [6]. The left plot shows the absolute current normalized to 0 °C and the right plot shows the current in the innermost three module groups normalized to the outermost module group that is composed of 3D sensors. The predictions in the left plot are after a χ^2 fit to the Φ/L_{int} scaling factor for each of the four module groups (represented by different colours). The z ranges of each group are indicated in the plots.

Similar figures for the outer three pixel layers (B-layer, L1, and L2) are presented in Fig. 39. Unlike the IBL, the outer layers have been active since the start of the LHC and so the current history spans nearly 200 fb^{-1}. The ratio between the various layers (right plot of Fig. 39) is nearly constant with time, as expected when both layers are fully depleted.

The fitted Φ/L_{int} scale factors for the IBL and the outer pixel layers are shown in Fig. 40 as a

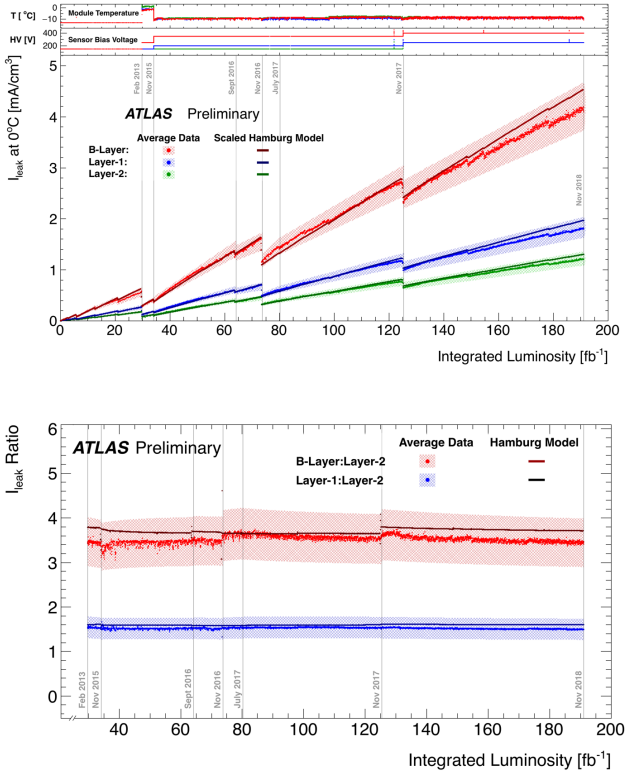

Fig. 39: The leakage current as a function of the integrated luminosity in Run 2 for the outer pixel layers of the ATLAS detector [11]. The top plot is the absolute current and the bottom plot shows the ratio between the inner layers and the outer layer. The predictions in the left plot are after a χ^2 fit to the overall Φ/L_{int} scaling factor per layer.

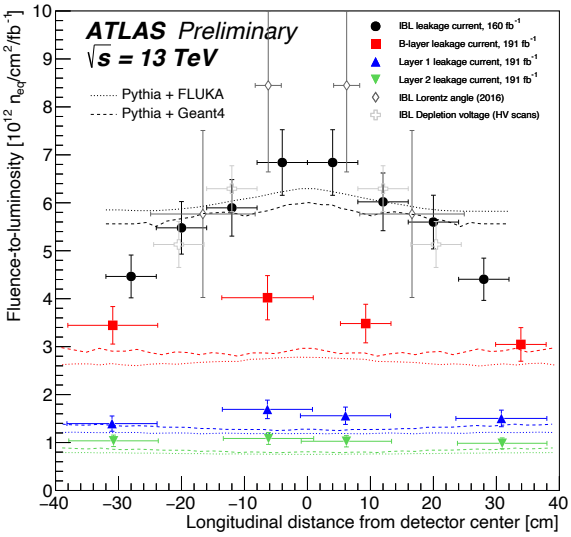

Fig. 40: The predicted fluence rates compared with the measured Φ/L_{int} scale factors [6, 11]. The different marker colours correspond to the four pixel layers. Extractions with other methods are presented and will be discussed in subsequent sections.

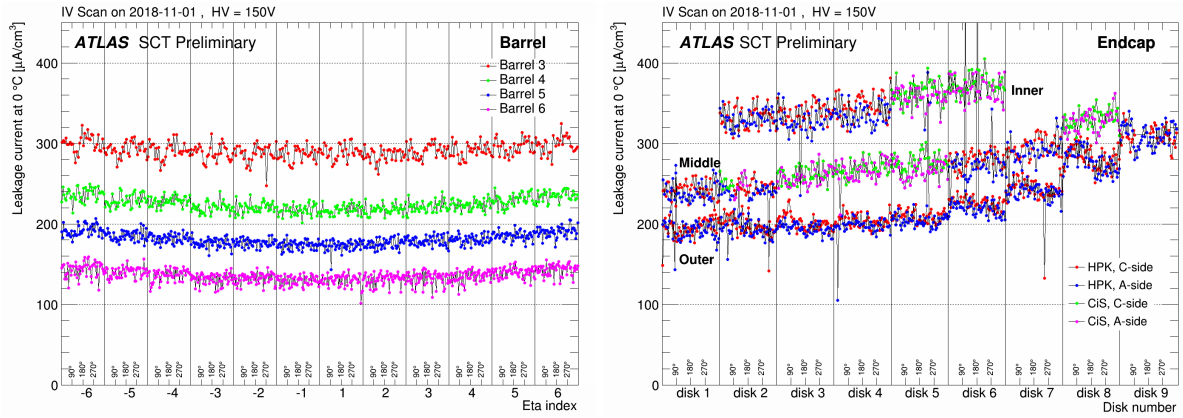

Fig. 41: A measurement of the leakage current on the ATLAS strip detector in the barrel (left) and disks (right) [12].

function of z. The innermost layers have acquired the most fluence and so are at the top of the plot. A large $|z|$-dependence in the IBL is observed in data that is not reproduced by the simulation. Furthermore, the overall fluence is about 50% higher in the outer layers compared with the simulation while the average fluence is approximately correct for the IBL. For reference, the IBL is at 3.3 cm while the B-layer is at 5.1 cm and the outer two layers are at 8.9 and 12.3 cm, respectively.

5.3.1.2 ATLAS strips

Leakage current measurements with the ATLAS strip detector are presented in Fig. 41. The current is nearly independent of z in the barrel detector while a significant increase in fluence is observed in the outermost disks. A comparison between the measured current in each barrel layer and predictions are shown in Fig. 42. The Hamburg and Sheffield models agree well with each other and with the data without a scale factor.

An increasing leakage current contributes to the module heating. As the leakage current itself depends strongly on the module temperature, this leads to a feedback loop. If this feedback loop does not converge from moderation with active or passive cooling, then thermal runaway can cause module failures. A study of thermal runaway is presented in Fig. 43. So far there is no indication of thermal runaway, but it may be necessary to operate the detector colder in Run 3.

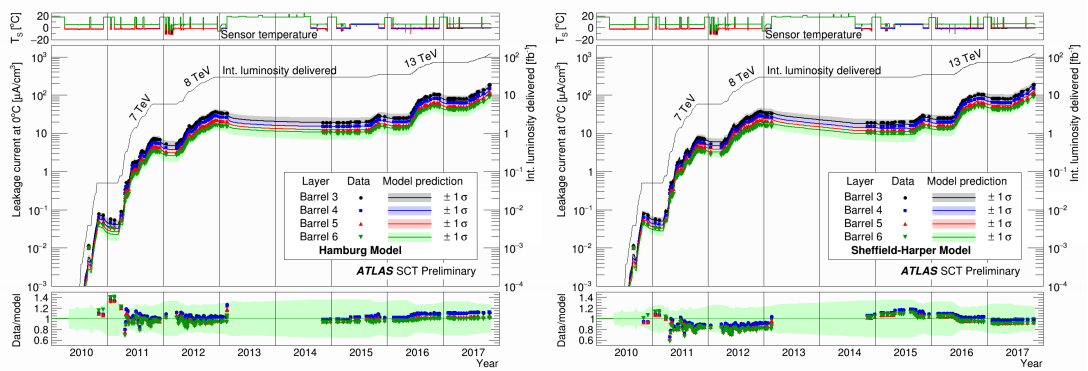

Fig. 42: A comparison of the measured and predicted leakage current as a function of time in the ATLAS strip detector [12] for the Hamburg model (left) and the Sheffield model (right). No scaling factor is applied to the leakage current predictions.

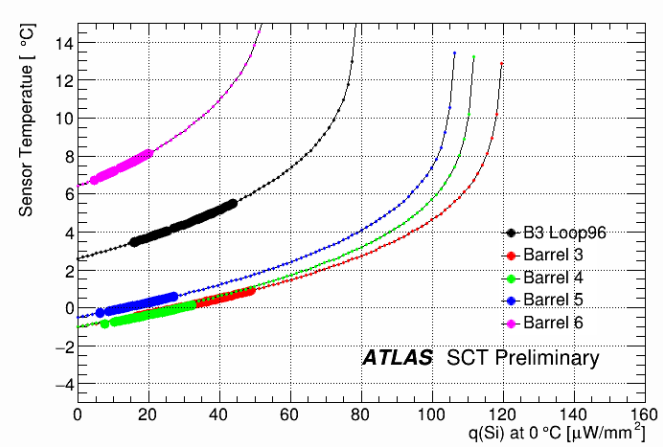

Fig. 43: A study of thermal runaway in the ATLAS strip detector [12]. The horizontal axis is the power per area while the vertical axis is the sensor temperature. The data points are large markers and the predictions are in small markers, extending to the expected conditions in 2023.

5.3.1.3 CMS pixels

The CMS pixel detector was replaced half-way through Run 2. Measurements and predictions of the leakage current for the new four-layer pixel detector are presented in Fig. 44. The measurements are taken for each LHC fill, 20 minutes into stable beam, excluding short or fills with small number of bunches. They are taken for all sectors and averaged for each layer excluding not operated modules. The averaged current corresponds to one module with a volume of $0.0285 \times 6.48 \times 1.62\ \text{cm}^3 \approx 0.3\ \text{cm}^3$. The simulations for each layer are performed for $z = 0$ and $r = 2.898$, 6.757, 10.8725, and 15.9805 cm for Layers 1 to 4, respectively. The simulated leakage currents are scaled to the temperatures at which the measurements were taken using Eq. 25 [8]. Scale factors are applied to the simulation to match the data. This scale factor is 1.0 for the innermost layer, 2.2 on the second layer, 2.0 on the third layer, and 1.8 on the outermost layer. After applying these scaling factors, the simulation provides an excellent model of the time dependence of the leakage current. The final fluences, derived using FLUKA, are 79, 18, 9 and $5 \times 10^{13}\ \text{n}_{\text{eq}}\text{cm}^{-2}$ for Layers 1 to 4, respectively.

Unlike ATLAS, the HV channels in CMS are grouped together in z so it is not possible to determine the z dependence of the leakage current during detector operations. Studies with the forward pixel detector (Fig. 45) do not show a $|z|$ dependence in either data or simulation which is approximately consistent with the outer pixel layer results from ATLAS. While the comparison of the $|z|$ dependence is inconclusive, the larger-than-expected fluence on the outer barrel layers is observed by CMS as well as ATLAS.

5.3.1.4 CMS strips

In the CMS strip detector leakage current, together with sensor temperature, is monitored at module level using the DCU on the front-end hybrid PCB. The leakage current of each module in the CMS strip detector in the middle of Run 2 is shown in Fig. 46. Inhomogeneities are due to degraded cooling in some parts of the detector. Measured values of leakage current are corrected for temperature variations and compared with Hamburg model predictions. The computed evolution is based on the global temperature and luminosity history. It takes into account the increase of the temperature expected from the increase in power dissipation with leakage current. Leakage current measured and predicted values are compared for each layer as a function of time and luminosity (Fig. 47). The predictions agree with the data within 20% and there is only a slight difference between Run 1 and Run 2. Differences are compatible with the uncertainties.

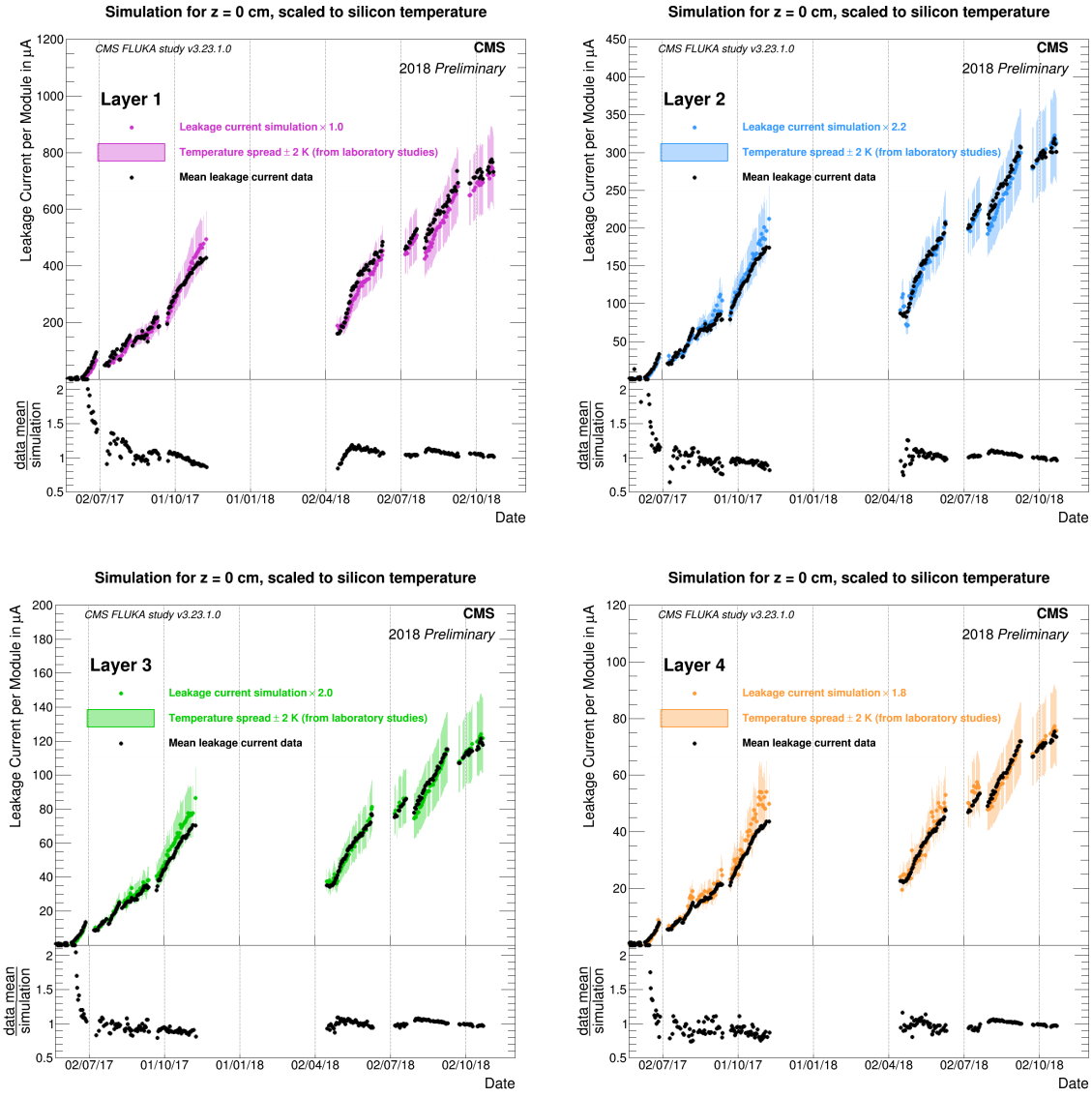

Fig. 44: Comparison of the measured leakage current per sensor module (approximately 0.3 cm^3 of silicon) with simulation for the four layers of the CMS barrel pixel detector. For Layers 2 to 4 the simulated values are scaled by a factor of about 2, as indicated on each of the three plots.

CMS has also investigated thermal runaway. A small number of modules already in Run 2 experienced thermal runaway due to degraded cooling contacts and relatively large fluences. In the example in Fig. 48 the currents from two HV channels connected to sets of modules from a double-sided layer are shown. When both channels are switched on thermal runaway occurs until one of the two channels trips due to reaching its current limit. One of the two HV channels can, however, continue to operate. The occurrence of further thermal runaways was limited in the last year of Run 2 by decreasing the baseline temperature between 15 and $-20\,^{\circ}\mathrm{C}$.

5.3.1.5 LHCb vertex detector

Even though the LHCb detector has received about a factor of 10 fewer collisions than ATLAS or CMS, the fluence on the VELO is comparable to the innermost pixel layers of ATLAS and CMS ($\sim 10^{15}\ \mathrm{n_{eq}/cm^2}$ after Run 2) due to the closer proximity to the collision point. Figure 49 shows the

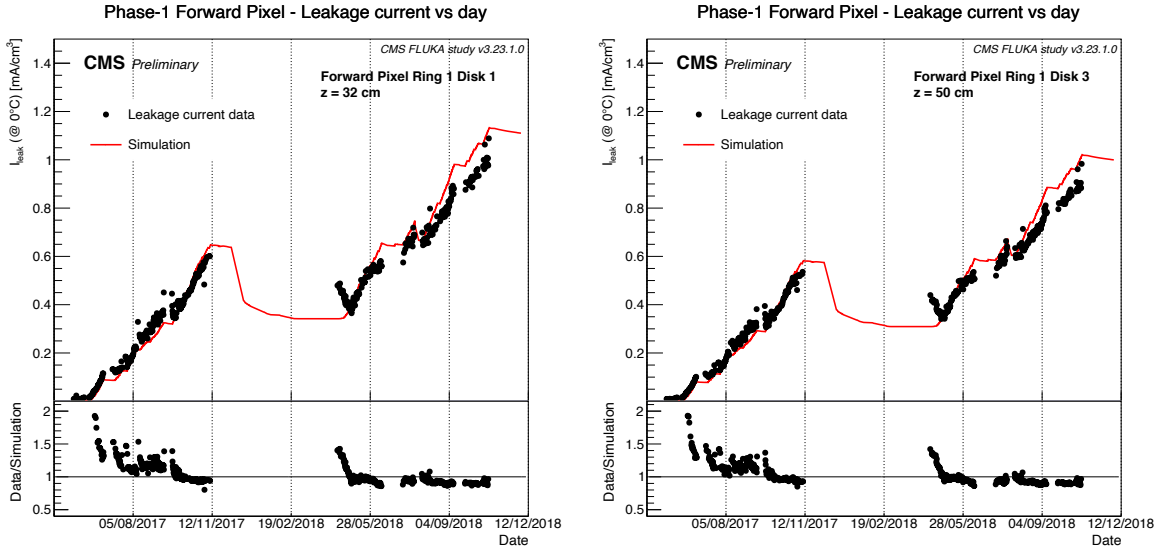

Fig. 45: A comparison of the measured and simulated leakage currents on the CMS forward pixels in 2017 and 2018 with a total of 120 fb^{-1}. The plots are for the inner ring (average radius 7.8 cm) and for the closest disk to the interaction (left) and the furthest disk from the interaction (right). No fluence-to-luminosity scaling factors are applied to the simulation.

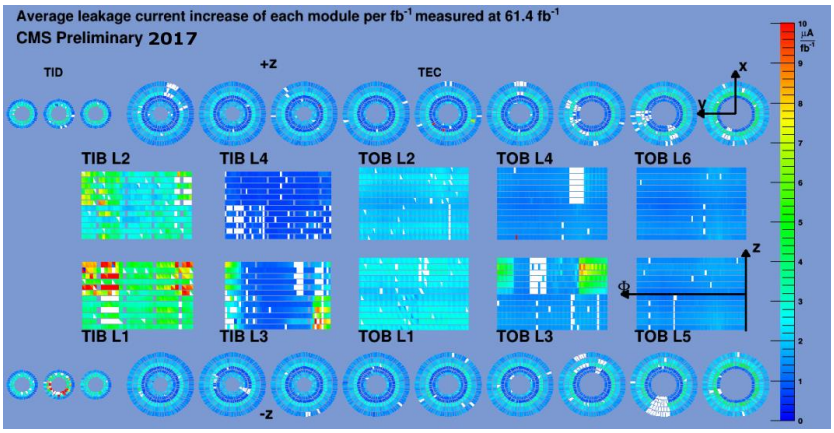

Fig. 46: The leakage current per module for the CMS strip detector in the middle of Run 2 (after 61.4 fb^{-1}). The middle rectangles show the barrel region and the disks are above and below. The currents shown here are not corrected for variations in the module temperature.

measured and predicated currents from the beginning of Run 1 through the end of Run 2. The Hamburg model provides an excellent model of the data across the entire VELO lifetime.

5.3.1.6 LHCb tracker turicensis

The current drawn by each HV channel in the LHCb tracker turicensis (TT) is monitored with a resolution of 1.0 μA, and a maximum interval of 120 minutes allowed between consecutive readings. The current for a given channel is defined as the maximum observed during a given LHC fill (typically several hours). Figure 50 shows how the measured leakage currents vary along the beam direction in z. Figure 51 presents the measured and predicted leakage current using the Hamburg model. The simulation provides an excellent model for the data across the entire TT lifetime.

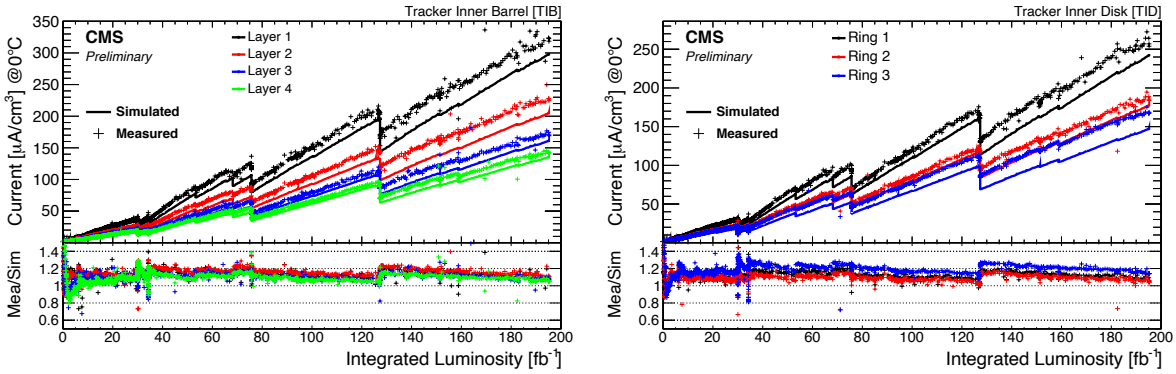

Fig. 47: The measured and predicated leakage current as a function of the integrated luminosity since early Run 1 for TIB (left) and TOB (right). The predictions are not scaled to match the data.

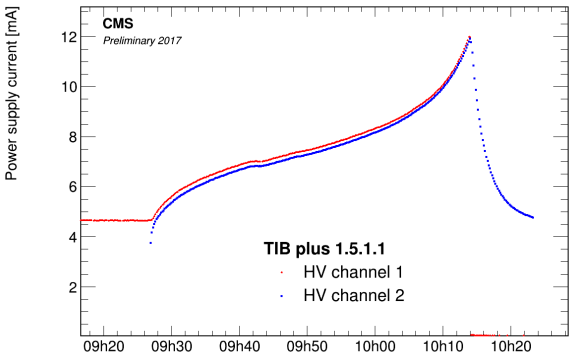

Fig. 48: An example of thermal runaway in Run 2 in one power group of the CMS strip detector

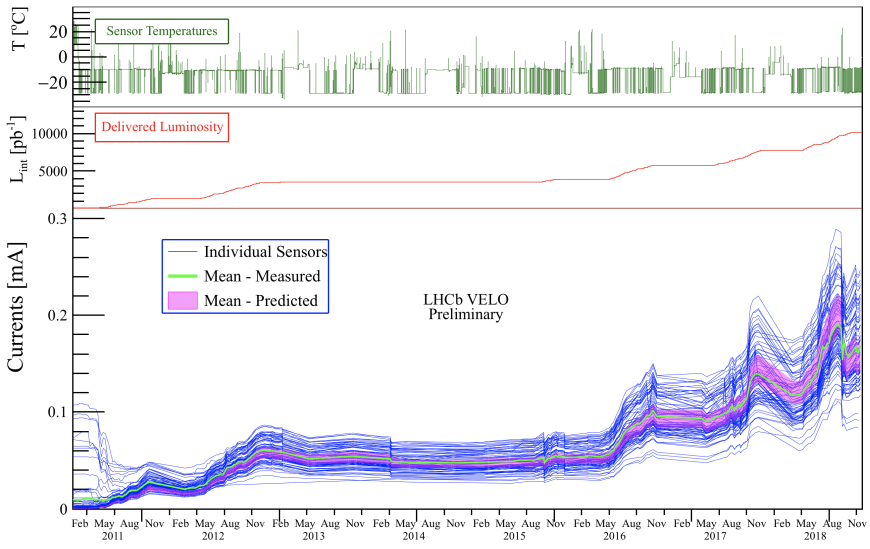

Fig. 49: The leakage current for the VELO sensors as a function of time scaled to 0 °C. The average measured and Hamburg model predicated currents are also shown.

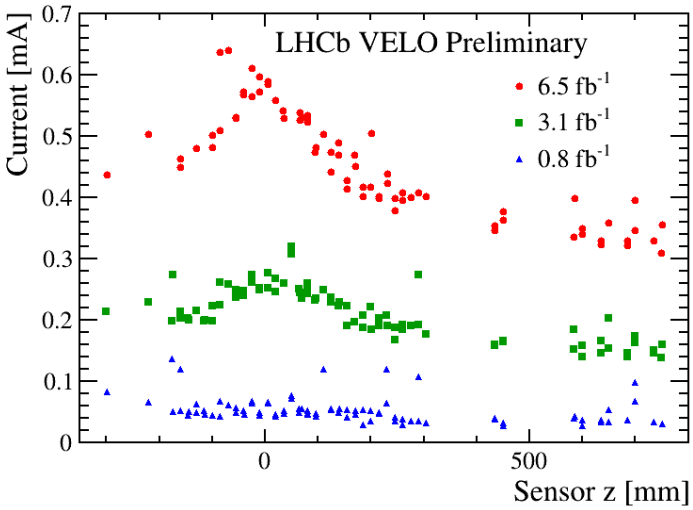

Fig. 50: The leakage current at various locations along the beam direction (z)

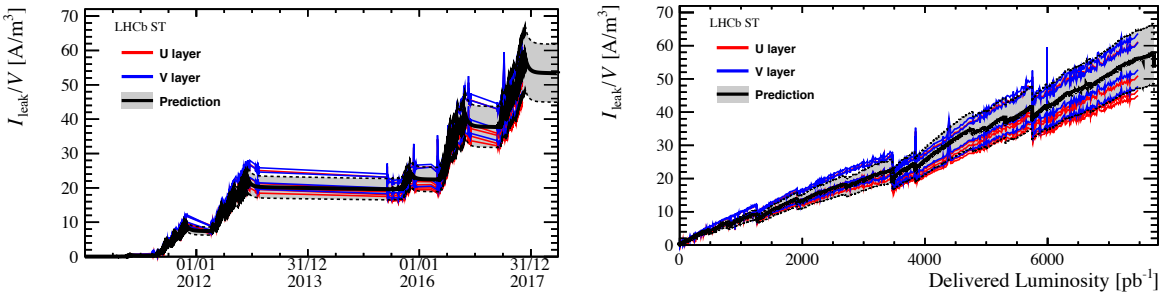

Fig. 51: The measured and predicated leakage current as a function of time (left) and integrated luminosity (right) for the innermost sensors in the second and third detection layers, indicated as U and V layers, respectively [7]. Currents are normalized to 8 °C. The grey uncertainty band includes uncertainty on the Hamburg model parameters, on the input FLUKA simulation, and on the temperature measurements. The effective band gap energy is set to 1.21 eV.

5.3.2 Depletion voltage

The depletion voltage is often determined by performing a scan of the collected charge or hit/cluster efficiency with applied high voltage. Unlike for leakage current, this requires that the depletion voltage be measured during collisions (or integrate for a long time with cosmic runs).

5.3.2.1 ATLAS pixels

Depletion voltage measurements and predictions from the Hamburg model in the innermost two layers of the ATLAS pixel detector are presented in Fig. 52. The IBL measurement includes the full Run 2 dataset while the B-layer measurement includes data from early Run 1 up to the middle of Run 2. The first measurements before space-charge-sign inversion were performed with cross-talk scans since the pixels were isolated. These scans are particularly useful because no active collisions are required. However, once the pixels are non-isolated following type inversion, this method is no longer available. Following space-charge-sign inversion, the depletion voltage is determined from charge collection efficiency scans. The measured charged versus high voltage is fit to a square root and linear function. The point where these two functions intersect is defined as the depletion voltage.

The introduction rates were fit to the Run 1 and early Run 2 data [6]. In order to fit these data, the

introduction rates g_Y and g_C were increased for the IBL with respect to the ROSE Collaboration values. While this fit provides a reasonable model of the Run 1 and early Run 2 data, it fails to describe the full Run 2 IBL leakage current. Various *ad hoc* modifications to the Hamburg model were investigated, but none resulted in global agreement with the data.

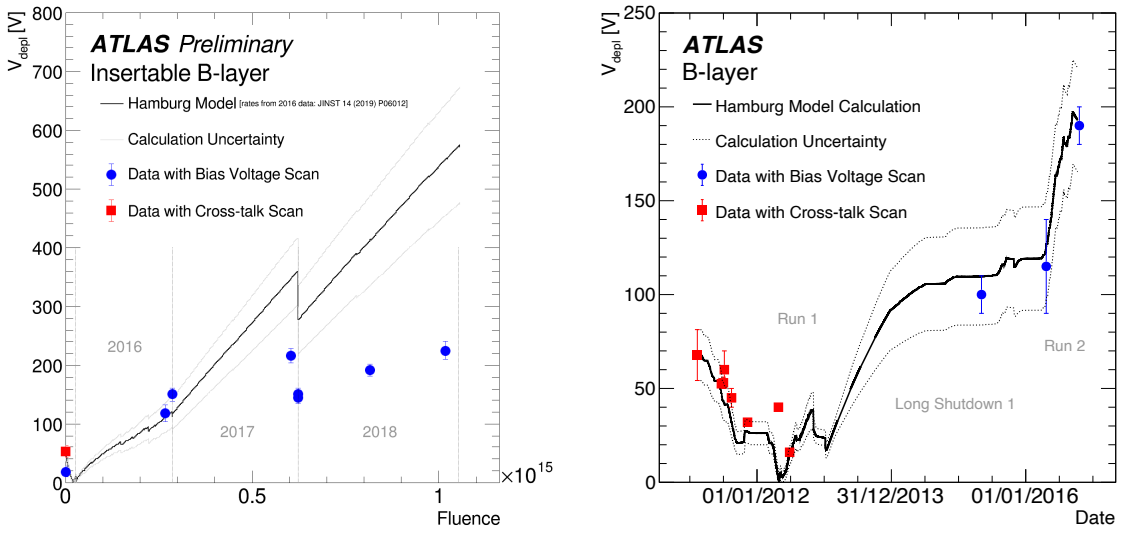

Fig. 52: Measurements and Hamburg model predictions for the ATLAS IBL (left) and B-layer (right). Circular points indicate measurements of the depletion voltage using the bias voltage scan method while square points display earlier measurements using cross-talk scans. The uncertainty band results from the fitted uncertainty in the introduction rates.

5.3.2.2 ATLAS strips

The ATLAS strip detector has a binary readout, so a charge collection scan cannot be used to determine the depletion voltage. Instead, a hit efficiency scan can be used (also studied with the average cluster size), as indicated in the left plot of Fig. 53. The increasing depletion voltage from the scans conducted in April and September of 2018 indicate that the sensors have passed space-charge-sign inversion. However, the efficiency starts to drop when going from high to low voltage at a much higher voltage (100 V) than the expected full depletion voltage (about 50 V).

5.3.2.3 CMS pixels

The average cluster charge and size are used to determine the full depletion voltage for the CMS pixel detector. Figure 54 presents measurements and Hamburg model predictions for the second half of Run 2 for the new pixel detector. For both measurement approaches, the full depletion voltage is estimated from the kink in the respective curves. The two measurement approaches show similar trends with time, but the actual measured full depletion voltage tends to be higher for the cluster charge determination than for the cluster size method. The depletion voltage was measured frequently during 2018 (about once/month) and the simulation under-predicts the outer layers and over-predicts the inner layer (similar to the ATLAS IBL).

Analogously, the full depletion voltage for the CMS forward pixel detector is determined from the average cluster charge. Figure 55 shows the evolution of the expected full depletion voltages for the forward pixel tracker disks based on the full temperature and irradiation history, as simulated using the Hamburg model. In this case the Hamburg model is fitted to 2018 data leaving g_C parameter as a free parameter. The g_Y parameter is fixed to 7×10^{-2} cm^{-1} and g_A to 1.4×10^{-2} cm^{-1}. The simulation

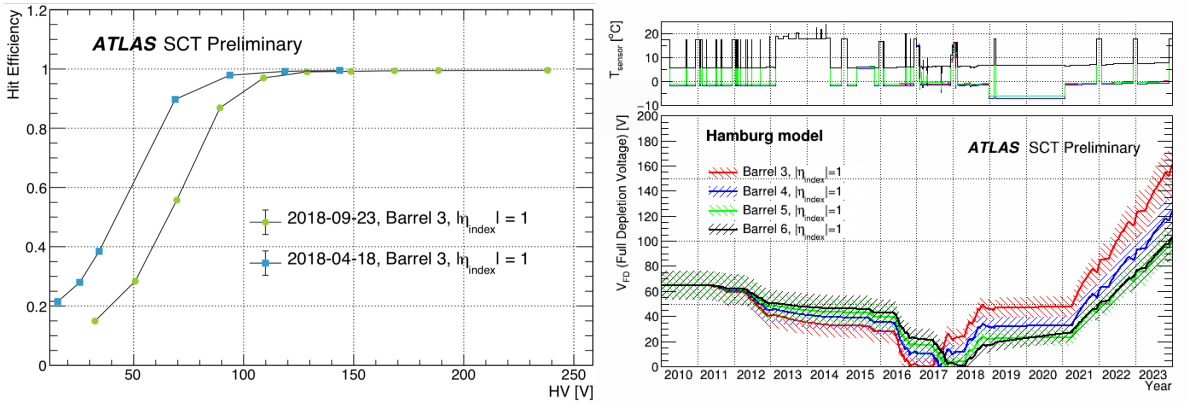

Fig. 53: A scan of the hit efficiency versus the sensor high voltage (left) and the simulated full depletion voltage using the Hamburg model for the four barrel layers [12]. Space-charge-sign inversion is predicated to have occurred during 2016.

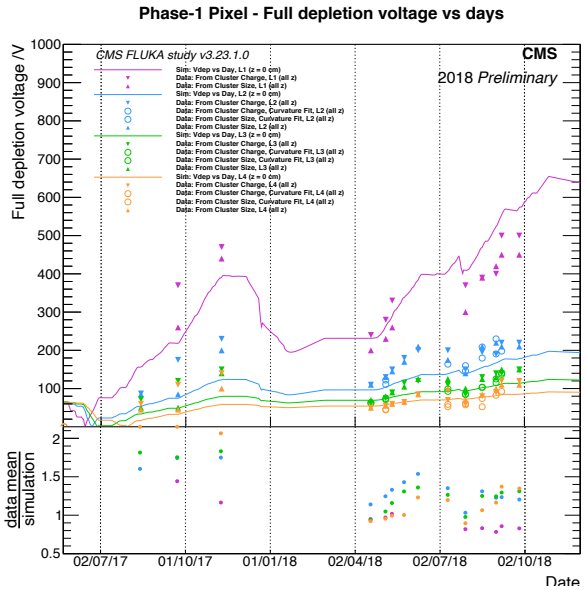

Fig. 54: Measurements and simulations of the full depletion voltage as a function of time since the start of 2017, when the new pixel detector was installed for the barrel layers 1 (purple), 2 (blue), 3 (green), and 4 (orange). Both cluster charge and cluster size measurements are used to determine the full depletion voltage.

well predicts the measurements in both the closer and farer disk from interaction point, except for the end of the Run 2, where predictions overestimate measurements. Figure 56 presents the comparison of the fit to the data following the Hamburg model performed assuming a linear or logarithmic dependence of the effective doping concentration on the fluence. This study shows that for the end of Run 2, a logarithmic trend better describes measurements. The fit method has been tested also on the barrel Layer 1 pixel detector, comparing the linear and logarithmic model, as presented in Fig. 57. For the Layer 1 the logarithmic model describes data much better, except for the period before type inversion.

5.3.2.4 CMS strips

As with the CMS pixel detector, both the cluster charge and width are used to determine the full depletion voltage for the CMS strip detector. It was found that the cluster width has a better sensitivity to low

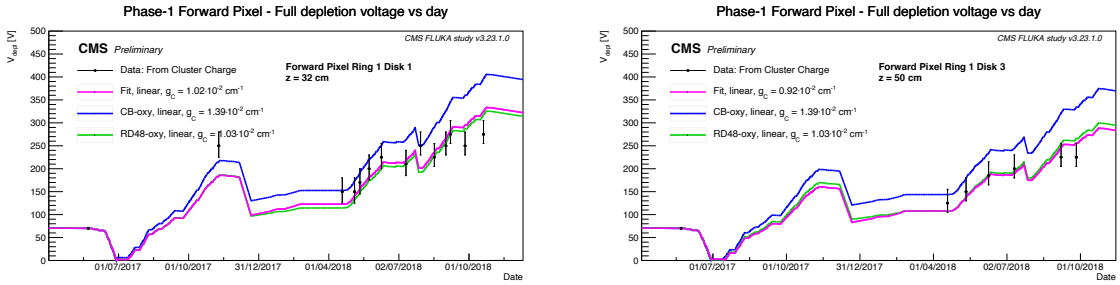

Fig. 55: Measurements and simulations of the full depletion voltage as a function of time since the start of 2017, when the new pixel detector was installed, for the inner ring (Ring 1) of two endcap disks (Disk 1 and Disk 3). Cluster charge measurements are used to determine the full depletion voltage. The resulting prediction (magenta line) is compared to the Hamburg model using two sets of Hamburg parameters for oxygenated Si (DOFZ): CB-oxy (blue line) and RD48-oxy (green line).

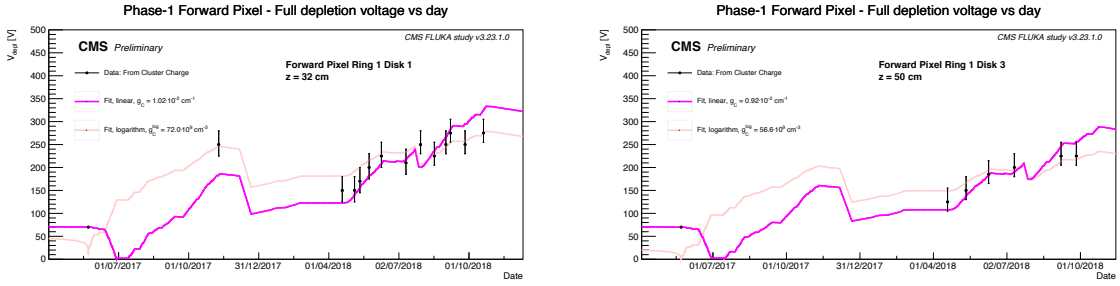

Fig. 56: Comparison of the fit to the data following the Hamburg model, with a linear (magenta) and a logarithmic (pink) dependence of the effective doping concentration on the fluence for the CMS forward pixel detector.

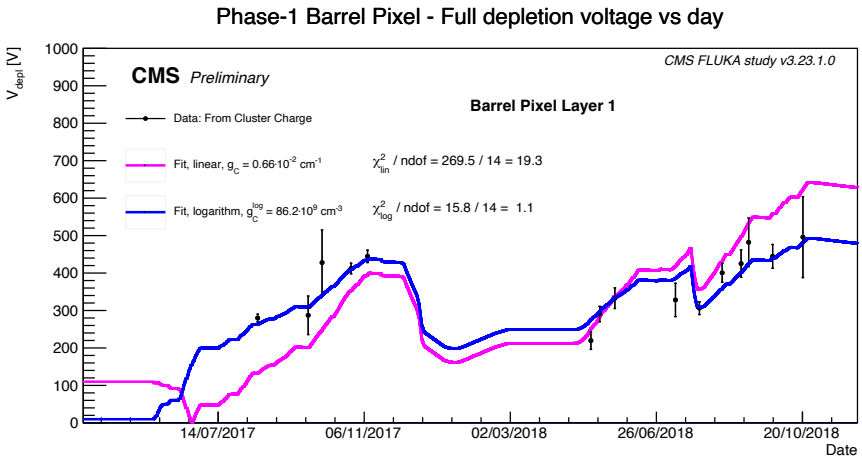

Fig. 57: Comparison of the fit to the data following the Hamburg model, with a linear (magenta) and a logarithmic (blue) dependence of the effective doping concentration on the fluence for Layer 1 CMS barrel pixel detector.

depletion voltages and is thus used for the baseline results presented in Figs. 58 and 60. The point of full depletion itself is determined by fitting the trend of average cluster width versus bias voltage to two linear curves. The point of intersection is the estimated bias voltage (Fig. 59). Scans are performed approximately four times per year.

A comparison between data and simulation for one module on the innermost strip layer is presented in Fig. 60 (left). At the end of Run 2, the sensors have just begun space-charge-sign inversion. Overall, the agreement between the data and the prediction are excellent, agreeing within about 10%. The experimental method loses sensitivity on the full depletion voltage at low values where many clusters cannot be reconstructed and very few steps are below the full depletion voltage. Most of the sensors start reaching doping inversion around the end of 2017. The evolution averaged over sensors of the same layers are provided until the end of 2017. As presented in Fig. 60 (right), the evolution scales with fluence and depends on the sensor thickness as the depletion voltage directly depends on the thickness.

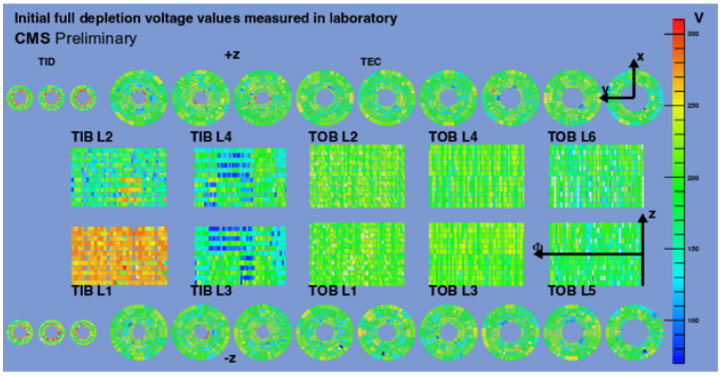

Fig. 58: The measured full depletion voltage for all CMS strip modules using CV curves prior to any irradiation.

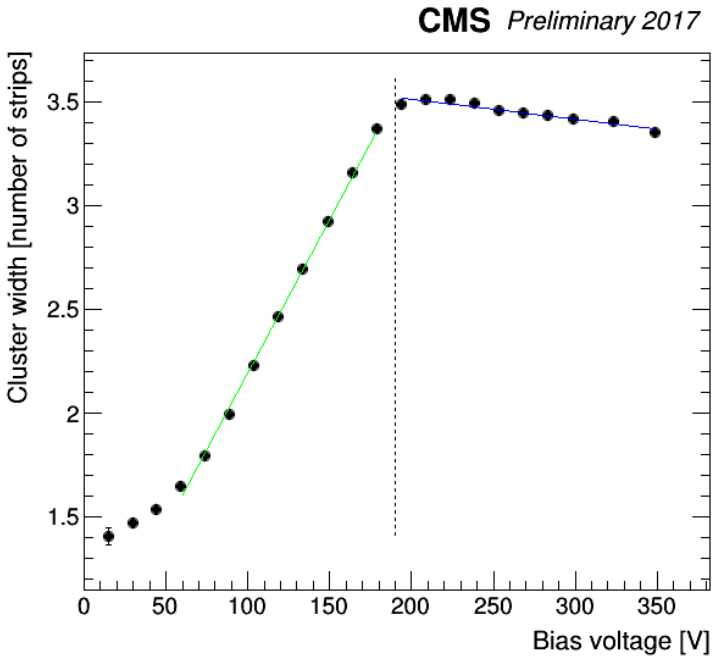

Fig. 59: Evolution of the cluster width as a function of the bias voltage. The saturation point is extracted from linear fits of the two regimes of the curve indicated in green and blue. Their crossing point gives the position of the full depletion voltage. See Ref. [3].

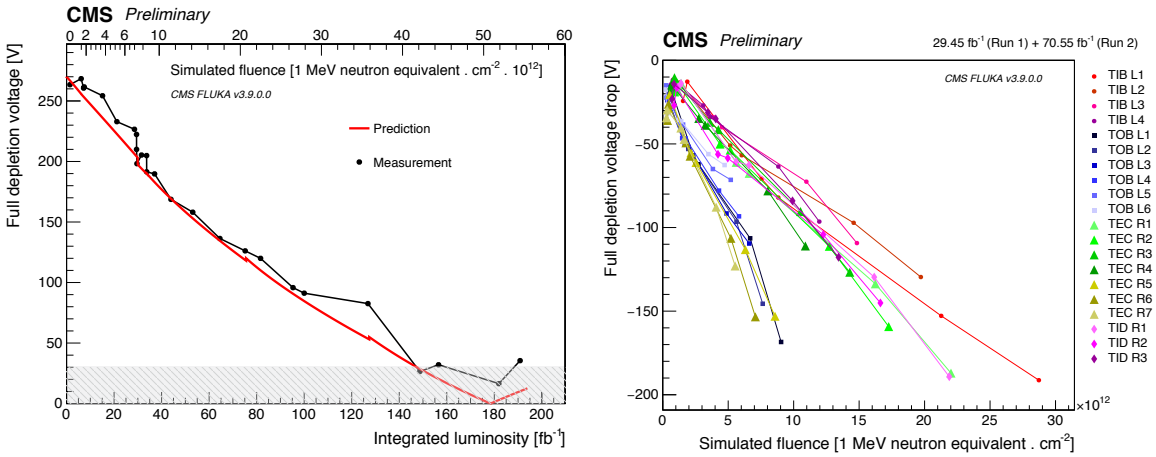

Fig. 60: Left: the measurement and prediction of the full depletion voltage in the CMS strip detector for a single module. The break in the simulation at about 30 fb^{-1} is due to an extended period at room temperature due to the opening of the CMS detector and cooling plant maintenance. Additional breaks at 75 and 130 fb^{-1} occur during winter shutdown periods. The grey area denotes regions where the signal-to-noise is too low so that no clusters are reconstructed in the rising part of the average cluster width curve. Right: the measured full depletion voltage including all power supplies of the CMS strip detector, with scans taken twice per year. The two sets of curves correspond to the two groups of sensors with different thicknesses (320 μm and 500 μm).

5.3.2.5 *LHCb vertex detector*

Since 2015, there have been 16 charge collection efficiency scans with 13 voltage steps each. These scans are performed during the normal data taking by varying the bias voltage on only every fifth sensor. Most sensors are in their standard operating voltage and thus the normal tracking algorithms can be executed, excluding the sensors with a varied bias voltage. The actual charge collection efficiency is estimated by fitting the distribution of analogue-to-digital counts to a convolution of a Landau and Gaussian. The *effective depletion voltage* is defined as the voltage at which the most probable value of the fitted probability density reaches 80% of its maximum value. Figure 61 shows the evolution of the effective depletion voltage as a function of time since the start of Run 1. The VELO was kept cold during all of the shutdown, which is why the depletion voltage is predicated to be constant. The sensors were purposefully heated near the end of Run 2 by changing the temperature from -30 to $-25\,^{\circ}$C for three days (during a technical stop). This engineered beneficial annealing reduced the effective depletion voltage by about 70 V, as indicated in Fig. 62. Decreasing the depletion voltage with purposeful heating is a potentially powerful technique, but also requires high-fidelity simulation tools.

5.3.2.6 *LHCb tracker turicensis*

The full depletion voltage for the LHCb TT detector is determined from charge collection efficiency scans. Such scans are performed two to four times per year, including just before the winter shutdown and at the beginning of the LHC operations in the spring. The whole scan takes 2–3 hours, with eleven different bias voltage steps. The actual charge used for the extraction is determined as the most probable value from a fit of two Gaussian distributions and two Landau distributions all convolved with each other and fit to the analogue-to-digital-conversion values. The second Landau is used to account for e^+e^- pairs from photon conversions that deposit twice as much charge as a single minimum ionizing particle. Integrating these most probable values over different time samplings results in an estimate of the total charge. The actual depletion voltage is determined using a fifth-order spline with a constant plateau. Figure 63 reports the predicted and measured full depletion voltage (defined as the voltage

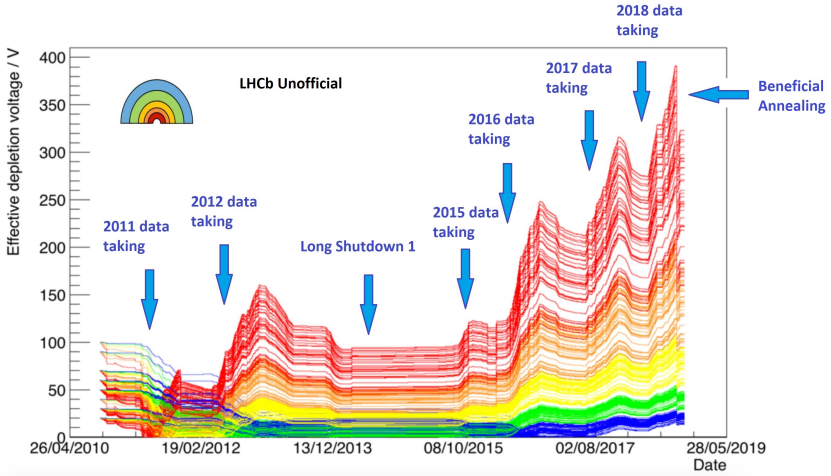

Fig. 61: The predicated full depletion voltage as a function of time since the beginning of Run 1 until the end of Run 2. Annotated arrows indicate LHC events, including periods of data taking and the long shutdown between Runs 1 and 2.

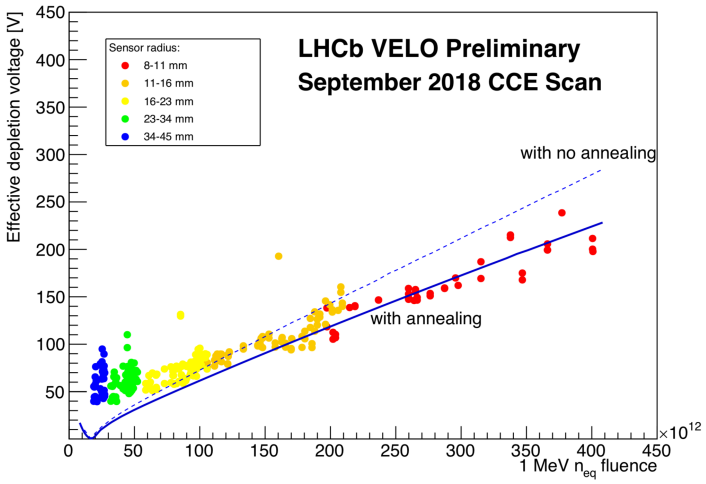

Fig. 62: The full depletion voltage as a function of fluence. Measurements are coloured based on their proximity to the interaction point. The impact of annealing is shown in the dashed line.

corresponding to 94% of the plateau value). Measurements and predictions as a function of fluence are presented in Fig. 64. At the time of the reported measurement, the sensors had not yet undergone space-charge-sign inversion.

Additional observables have been studied to probe the detector response to non-ionizing energy loss. modelling these observables is more complicated than for the leakage current and full depletion voltage because they require a simulation of the electric field profile inside the sensor bulk. While all of the silicon systems in ATLAS, CMS, and LHCb have measured the leakage current and depletion voltage, the catalogue of additional measurements is not as complete. Therefore, many of the following sections show measurement highlights from only one or two experiments.

5.3.3 Hit/cluster efficiency

The charge and hit efficiencies are often studied only during bias voltage scans, but can also be monitored during normal data taking conditions. Figure 65 shows the measured hit efficiency in the innermost layer

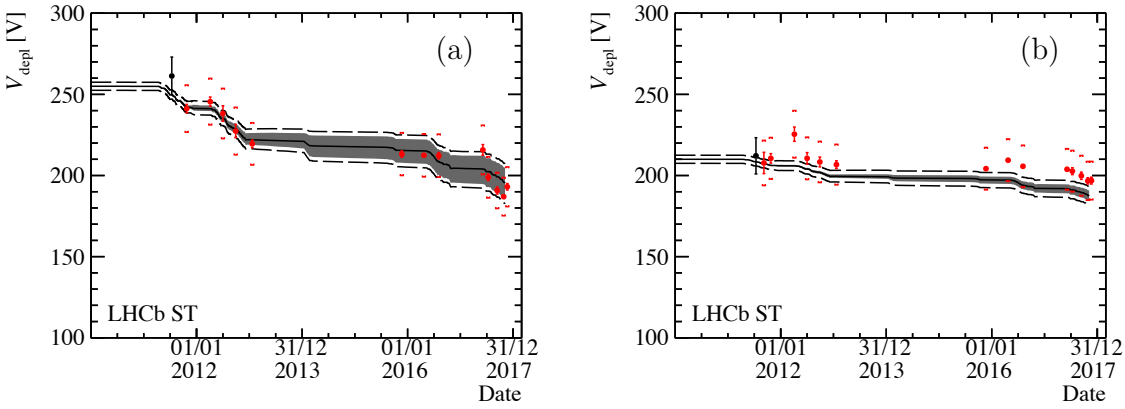

Fig. 63: The full depletion voltage in the LHCb tracker turicensis as a function of time [7]. The left plot is for sensors closer to the beam pipe (left) and further away from the beam pipe (right). The uncertainty band on the Hamburg model prediction corresponds to uncertainty in the model parameters while the black dashed band represents the uncertainty in the initial depletion voltage.

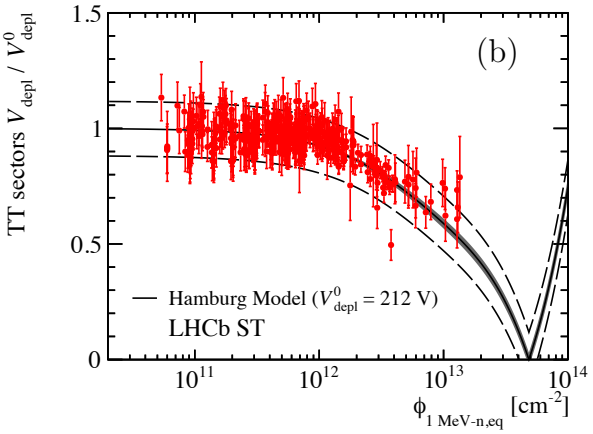

Fig. 64: The measured and predicted depletion voltage as a function of fluence in the LHCb tracker turicensis [7]. The black solid curve shows the predictions from the stable damage part of the Hamburg model and the band represents the model parameter uncertainty. This prediction is averaged over all sensors and the dashed line shows the standard deviation of the distribution of the initial full depletion voltages.

of the ATLAS strip detector in 2018. A 1% drop in the efficiency was recovered when the high voltage was adjusted from 150 V to 250 V after about 45 fb^{-1}.

The LHCb VELO community has also extensively studied the efficiency. One surprise, shown in Fig. 65 is that there are regions of low efficiency in the regions furthest away from the collisions (lowest fluence) that form after irradiation. This loss in efficiency has been connected with the second metal layer effect (see Ref. [13] for details). LHCb also took advantage of a unique opportunity at the end of Run 2. Since the VELO operation ended in Run 2 (replaced with a new detector for Run 3), potentially destructive high voltage scans were performed to determine how much the cluster finding efficiency could be recovered as well as probe for thermal runaway. The design voltage of the power supplies is only 500 V, but scans were conducted up to 700 V. The results of this study are shown in the right plot of Fig. 66. There is a drop in the efficiency for the innermost part of the detector that is recovered when the high voltage is increased. Going from 500 to 700 V actually increases the efficiency by about 2%.

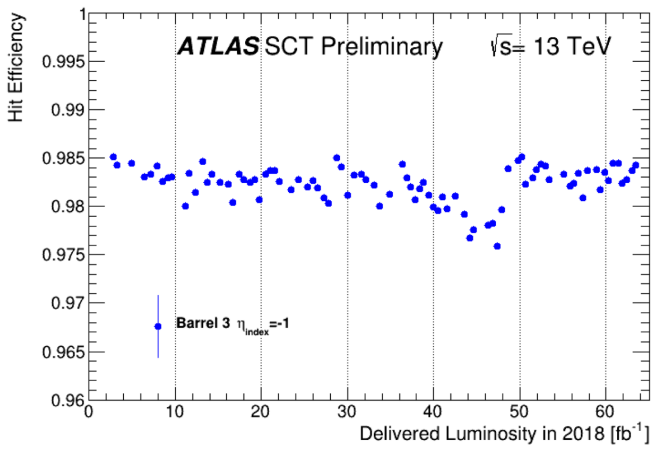

Fig. 65: The measured hit efficiency on the innermost barrel layer of the CMS strip detector in 2018 just before and after the high voltage was increased.

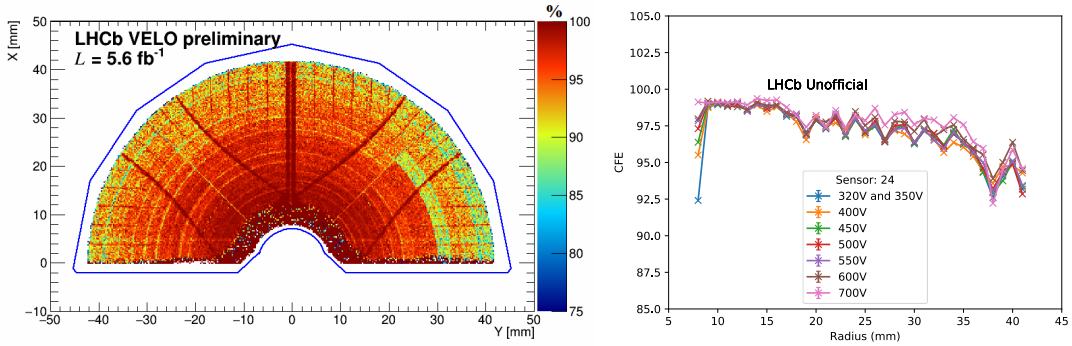

Fig. 66: Left: the cluster finding efficiency map as a function of location inside one of the VELO sensors. The position of the straight dark lines agree with the position of routing lines. Right: the cluster finding efficiency during the final high voltage scan at the end of Run 2 as a function of radius inside the LHCb VELO sensors.

5.3.4 Collected charge

While the impact of charge trapping on the hit efficiency is $\mathcal{O}(1\%)$ over Run 2, the impact on the collected charge can be much larger, $\mathcal{O}(10\%)$. Figure 67 presents a measurement of the measured charge and cluster size throughout Run 2 for the innermost layer of the ATLAS pixel detector. Jumps in the pixel cluster properties are due to changes in the operational conditions, most notably the high voltage. During periods of constant conditions, the charge and cluster size decreases with integrated luminosity. About 30% of the charge is now lost after the full Run 2.

5.3.5 Lorentz angle

The Lorentz angle depends strongly on temperature, but is also sensitive to deformations in the electric field within a sensor. One benefit of the Lorentz angle over other quantities like the charge collection efficiency is that the Lorentz angle is largely insensitive to charge trapping and instead directly probes the bulk electric field. Figure 68 shows the measured Lorentz angle for the ATLAS IBL detector throughout Run 2. During periods of constant temperature, the Lorentz angle is observed to be approximately proportional to the fluence. The fitted values of the response $\partial\theta_L/\partial\Phi$ are presented in Table 11. When

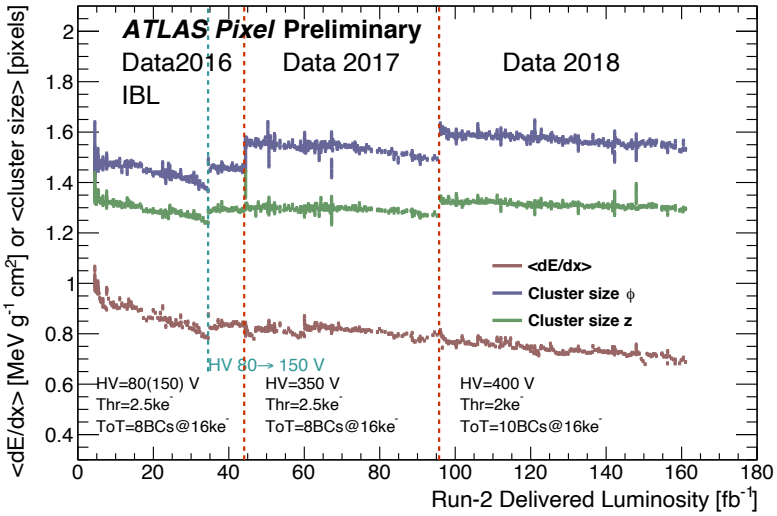

Fig. 67: The measured charge, longitudinal cluster size (z), and transverse cluster size (ϕ) as a function of the delivered integrated luminosity in Run 2 for the ATLAS IBL.

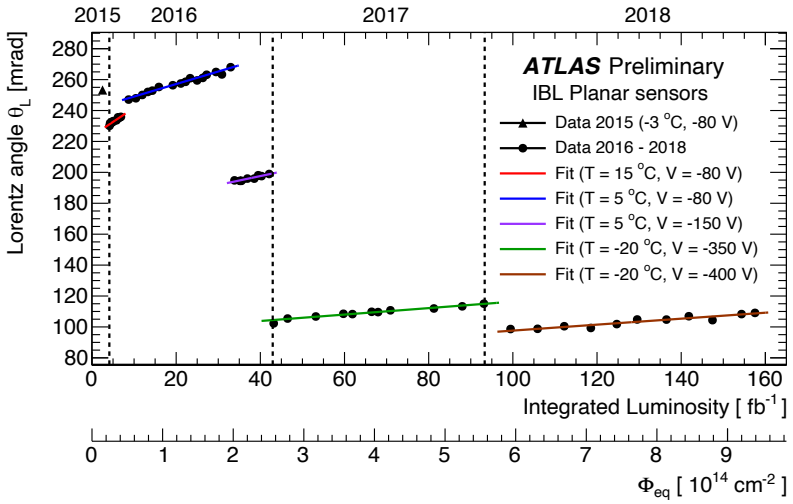

Fig. 68: The measured Lorentz angle during Run 2 in the ATLAS IBL

keeping the voltage constant, lower temperatures yield to smaller slopes. When keeping the temperature constant, higher voltages yield to smaller slopes.

5.3.6 Position resolution

The single cluster position resolution is sensitive to degraded charge information from charge trapping, mostly on the periphery of clusters due to lost hits. One challenge with *in situ* measurements of the single cluster position resolution is that they suffer from a large extrapolation/interpolation resolution that can mask subtle time-dependent effects. An alternative approach deployed by ATLAS for the IBL detector makes uses of overlapping modules [14,15]. In particular, the position resolution can be determined from a single layer for particles that traverse two modules on the same layer. Figure 69 presents a measurement of the corresponding resolution throughout most of Run 2 for the IBL detector. The slight worsening of the spatial resolution observed over the three years is correlated with the reduction of charge collection efficiency as a result of radiation damage. This may have important implications for flavour tagging

Table 11: Summary of the values for the intercepts and slopes obtained from linear fits to the Lorentz angle as a function of the fluence for fixed temperature T and high voltage V.

Temperature	Voltage	$\theta_L(\Phi_{\mathrm{eq}} = 0)$ (Mrad)	$(\partial\theta_L/\partial\Phi_{\mathrm{eq}})_{T,V}$ (Mrad·cm^2)
15 °C	80 V	223.5 ± 1.0	$(30.6 \pm 3.0) \cdot 10^{-14}$
5 °C	80 V	240.9 ± 0.7	$(13.6 \pm 0.6) \cdot 10^{-14}$
	150 V	174.6 ± 3.6	$(9.6 \pm 1.6) \cdot 10^{-14}$
−20 °C	350 V	95.5 ± 1.3	$(3.5 \pm 0.3) \cdot 10^{-14}$
	400 V	78.3 ± 2.8	$(3.2 \pm 0.4) \cdot 10^{-14}$

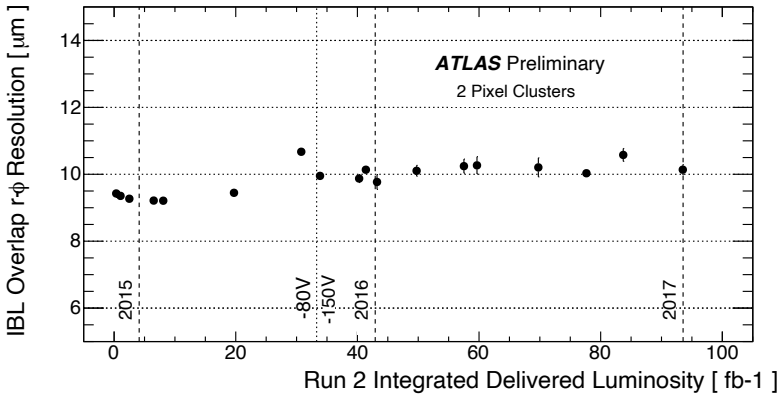

Fig. 69: The measured position resolution on the ATLAS IBL as a function of integrated luminosity during Run 2 [14, 15].

and other downstream track reconstruction tasks that depend on a precise position measurement on the innermost layer.

5.4 Discussion and outlook

Measurements of silicon detector response to non-ionizing energy loss is essential for every facet of data collection, analysis, and future planning. The previous sections have shown that there is an extensive measurement program from ATLAS, CMS, and LHCb, with a variety of important and unforeseen results. However, there are also many challenges associated with performing and interpreting these results. While many of these challenges are not often discussed in public documentation, they are critically important for improving methods and planning for the future. This is not exhaustive.

1. *Leakage current*: on the measurement side, it is not 100% clear how to define the leakage current. In theory, the current should raise, plateau, and then raise again as the high voltage is increased from zero up through breakdown. The current at the plateau region is the theoretical definition of the leakage current. The left plot of Fig. 70 shows a typical IV scan. While the current does level off beyond some voltage, there is no region where it is flat. This results in (an often unaccounted for) uncertainty in the reported current. Furthermore, the current depends strongly on temperature, as shown in the right plot of Fig. 70. This leads to a challenge because the temperature on the sensors is often not known precisely. In many cases, the temperature is measured far from the sensors and inferred from simulations or auxiliary measurements. This affects both the leakage

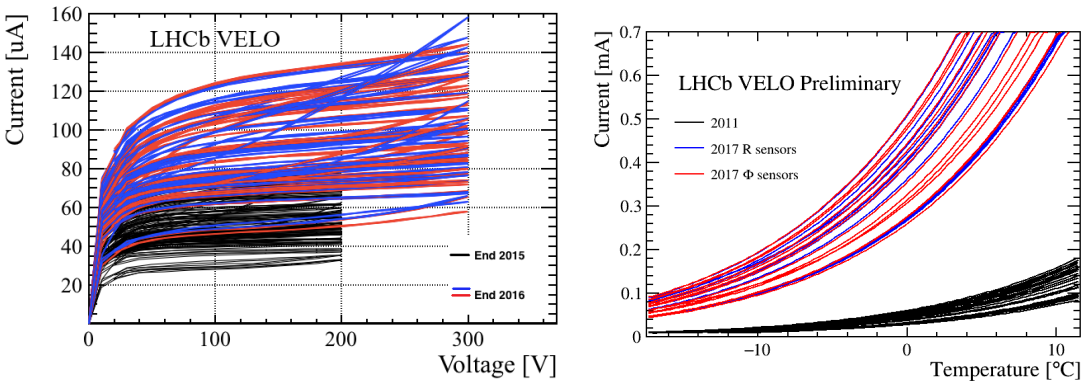

Fig. 70: Example current–voltage (IV) (left) and current–temperature (IT) (right) scans for the LHCb VELO detector [13].

current estimates and their interpretation because both require the measured temperature as input. A further complication is that the effective bandgap energy E_{eff} from Eq. 25 seems to anneal and may behave differently for charged/neutral hadron irradiation. For the interpretation, the α_j values in Eq. 21 have a significant unaccounted uncertainty related to damage factors used to converge between proton or pion fluxes and 1 MeV n_{eq}. There is also ambiguity in how to model periods of non-constant temperature. Despite these challenges, the time dependence of the leakage current modelling appears to be accurate across experiments and across detector layers.

2. *Depletion voltage*: as with the leakage current, there is a large ambiguity in the definition of the full depletion voltage. For scans of the collected charge or cluster size, the actual values do not saturate, so an *ad hoc* definition must be used (often fitting two lines and taking the kink position). As the previous sections have highlighted, each experiment and detector subsystem has a different definition. In fact, the full depletion voltage is not even well defined at high fluence when the electric field can have regions of low field within the bulk. As most measurements of the depletion voltage require active collision conditions, they are performed infrequently to not interfere with data collection for physics analysis. This makes it difficult to constrain and tune simulation models. On the simulation side, there is currently no model that includes both annealing and non-trivial depth-dependent doping concentrations. This could be one reason why both ATLAS and CMS see significant deviations between model and measurement towards the end of Run 2. Fortunately, the simulations over-estimate the measurements and thus are conservative. Additional challenges with the predictions arise from the fact that the introduction rates are not well known for charged and neutral hadrons. There is a strong need for the community to develop an improved model for depletion voltage in Run 3 and beyond. The notion of full depletion may not be well-defined, but each detector needs to pick a bias voltage for safe and effective operations.
3. The other observables introduced in previous sections have similar challenges, with further complications on the interpretation because a full detector simulation is required.

Despite the challenges with the interpretation of the data presented in the chapter, there are a variety of important messages from the extensive measurement campaign from all of the LHC experiments. In particular:

– the silicon leakage current predictions are in general in good agreement with measurements at the LHC experiments. However, the simulated 1 MeV neutron equivalent fluence seems to underestimate the pixel data in the region 5–15 cm from the interaction point. The reason for this is not yet understood. Nonetheless, the uncertainties associated with the model predictions are now much better constrained and understood, giving increasing confidence of predictions at the LHC

upgrades. See also Section 4.5;

- the Hamburg model for annealing agrees with the time dependence of the leakage current data to within about 10% (ignoring the overall offset described in the previous bullet), although there are indications that it may no longer be precise enough at the end of the LHC. The depletion voltage data are harder to model and work will be required to make this a precise predictive tool for the future;
- despite the extensive radiation damage, track reconstruction remains relatively robust and the current impact on physics analysis is relatively minimal. As the probability of a charge to be trapped becomes $\mathcal{O}(1)$, radiation damage effects will be a non-negligible challenge for our tracking detectors;
- as various detectors have been or are being upgraded, there is a unique opportunity to stress test the detectors in order to take valuable diagnostic data. This was demonstrated by the LHCb experiment in their final high-voltage scan of the VELO detector before it was decommissioned.

To summarize, this section has reported various measurements of the silicon sensor response to non-ionizing radiation from collisions in the LHC. A variety of probes have resulted in a detailed diagnostic information that can be used for modifying models, guiding operation and upgrades, as well as improving the quality of offline reconstruction. Expanding and enhancing this measurement program into Run 3 and the HL-LHC will be critical for preserving and possibly enhancing physics analysis as radiation damage becomes even more prominent. Addressing the challenges outlined in this section will involve community collaboration and sharing of ideas, which has already begun as a result of the workshop series that inspired this report.

References

[1] G. Avoni *et al.*, *JINST* **13** (2018) P07017, doi:10.1088/1748-0221/13/07/P07017.

[2] M.P. Rauch, Ph.D. thesis, RWTH Aachen University, 2020, doi:10.18154/RWTH-2020-05630.

[3] N. Tonon, Search for the associated production of a single top quark and a Z or Higgs boson with the CMS experiment, Thèse de Doctorat, 2019STRAE022, Université de Strasbourg, 1er Octobre 2019.

[4] M. Moll, Radiation damage in silicon particle detectors: Microscopic defects and macroscopic properties, Ph.D. thesis, Hamburg Univ., 1999, DESY-THESIS-1999-040.

[5] R.S. Harper, Radiation Damage Studies of Silicon Detectors and Searching for an Intermediate Mass Higgs Boson at ATLAS, PhD thesis, Univ. Sheffield, 2001.

[6] ATLAS Collaboration, *JINST* **14** (2019) P06012, doi:10.1088/1748-0221/14/06/P06012,

[7] C. Abellan Beteta *et al.*, *JINST* **15** (2020) P08016, doi:10.1088/1748-0221/15/08/P08016.

[8] A. Chilingarov, Temperature dependence of the current generated in Si bulk. *JINST* **8** (2013) P10003, doi:10.1088/1748-0221/8/10/p10003.

[9] ROSE Collaboration, 3rd RD48 status report, CERN-LHCC-2000-009 (CERN, Geneva, 2009).

[10] S.I. Parker, C.J. Kenney, J. Segal, *Nucl. Instrum. Methods Phys. Res.* **A395** (1997) 328, doi:10.1016/S0168-9002(97)00694-3.

[11] ATLAS Collaboration, Measurement of radiation damage through leakage current monitoring of the ATLAS pixel detector, ATL-INDET-PUB-2019-001 (CERN, Geneva, 2019).

[12] ATLAS Collaboration, SCT radiation damage plots, prepared for Radiation damage workshop, ATL-SCT-2019-001; K Mochizuki, Sensor measurements with the ATLAS SCT, Radiation effects in the LHC experiments and impact on operation and performance, CERN, 11–12 Feb. 2019, Indico.

[13] K. Akiba *et al.*, *IEEE Trans. Nucl. Sci.* **65** (2018) 1127 doi:10.1109/TNS.2018.2824618.

[14] ATLAS Collaboration, IBL hit spatial resolution, ATL-PIX-2018-002 (CERN, Geneva, 2018).

[15] ATLAS Collaboration, IBL efficiency and single point resolution in collision events, ATL-INDET-PUB-2016-001 (CERN, Geneva, 2016).

[16] ATLAS Collaboration, *JINST* **9** (2014) P08009, doi: 10.1088/1748-0221/9/08/P08009.

[17] ATLAS Collaboration, Luminosity determination in pp collisions at $\sqrt{s} = 13$ TeV using the ATLAS detector at the LHC, ATLAS-CONF-2019-021 (CERN Geneva, 2019).